Available online at www.sciencedirect.com
ScienceDirect
Journal of Catalysis 243 (2006) 329–339
JOURNAL OF CATALYSIS
www.elsevier.com/locate/jcat

Structure and reactivity of Pt–Ru/SiO_2 catalysts for the preferential oxidation of CO under excess H_2

Soo Yin Chin, Oleg S. Alexeev, Michael D. Amiridis *

Department of Chemical Engineering, University of South Carolina, Columbia, SC 29208, USA

Received 29 May 2006; revised 8 August 2006; accepted 9 August 2006

Available online 15 September 2006

Abstract

SiO_2-supported Pt–Ru bimetallic catalysts subjected to two different types of pretreatment protocols (i.e., subsequent oxidation–reduction treatments at 300 °C and direct reduction in H_2 at 300 °C) were characterized by extended X-ray absorption fine structure spectroscopy (EXAFS), scanning transmission electron microscopy (STEM), Fourier transform infrared spectroscopy (FTIR) of adsorbed CO, and catalytic activity measurements for the preferential oxidation of CO in the presence of excess H_2 (PROX). The EXAFS data show that both treatments led to the formation of dispersed bimetallic structures, with an average Pt–Ru bond distance of 2.68 Å. The close proximity between Pt and Ru helped stabilize Ru in a highly dispersed form and prevented its sintering after oxidation treatments. The FTIR results indicate that the adsorption of CO was substantially weaker on bimetallic samples than on the corresponding monometallic ones. Interparticle segregation (i.e., segregation of the two metals into individual particles) was observed with the Pt–Ru/SiO_2 sample exposed to direct H_2 treatment; in contrast, intraparticle segregation (i.e., segregation of the two metals within the same particle), with Pt preferentially occupying more surface sites, was observed when consequent O_2/H_2 treatments were used. As a result, the direct H_2 treatment yielded samples with PROX activity almost identical to that of monometallic Ru catalysts, whereas the O_2/H_2 treatment yielded samples with PROX activity intermediate to those of monometallic Pt and Ru catalysts.

Keywords: Selective oxidation; CO oxidation; PROX; Pt; Ru

1. Introduction

The activity of supported monometallic Pt and Ru catalysts for the preferential oxidation of CO in the presence of excess H_2 (PROX) has been extensively investigated [1–3]. The high activity and selectivity of these monometallic catalysts in PROX is often related to the saturation of metal surfaces by CO, which prevents H_2 adsorption and oxidation [4,5]. Under similar experimental conditions, the light-off temperature for Pt is approximately 200 °C, whereas Ru is known to be active in a lower temperature range (i.e., below 150 °C) [1,6–12]. Furthermore, Ru is known to have a slightly higher selectivity under limiting O_2 conditions (i.e., twofold stoichiometric amount, $O_2/CO = 1$). Therefore, it can be suggested that when both Ru and Pt are present in the catalyst formulation, the formed bimetallic catalyst could have a wider operation window and higher activity and/or selectivity for PROX than its monometallic counterparts. However, the number of reports describing the catalytic properties of Pt–Ru bimetallics for PROX is very limited [13].

Nevertheless, Pt–Ru/SiO_2 catalysts have been investigated for other reactions, such as CO methanation, hydrogenolysis of methylcyclopentane, and isomerization of 2-methylpentane [14,15], but these reports have not yielded an undisputed model for the structure of the supported bimetallic species. For example, whereas some authors have reported the formation of bimetallic Pt–Ru particles following reduction in H_2 [16,17], others have reported partial phase segregation under similar conditions [18]. There have also been reports of a core–shell-type model with a Ru-rich core and a Pt-rich outer shell [19–21]. Finally, there has been disagreement on whether an oxidation treatment before reduction could result in increased interactions between Pt and Ru [19,20,22].

More recent reports on the Pt–Ru bimetallic system have focused on the electrocatalytic application of this system for

* Corresponding author.
E-mail address: amiridis@engr.sc.edu (M.D. Amiridis).

0021-9517/$ – see front matter
doi:10.1016/j.jcat.2006.08.004

hydrogen oxidation due to its high activity [23–25] and high resistance to CO poisoning [26] compared with conventional Pt electrocatalysts. However, it is a common practice in electrochemical applications to use high loadings of the precious metals (i.e., 20–40%) to achieve the desired performance characteristics. Therefore, the structures of these catalysts are not representative of those encountered in heterogeneous catalysis applications, which normally use much lower loadings (i.e., 1–2 wt%) of the noble metals.

In this paper, we report the results of the oxidation of CO in the presence of excess H_2 over SiO_2-supported bimetallic Pt–Ru catalysts prepared by incipient wetness impregnation and subjected to different pretreatment protocols. EXAFS, STEM, and FTIR measurements of adsorbed CO were used to characterize the samples and allowed us to develop a structural model for the bimetallic structures present.

2. Experimental

2.1. Sample preparation

Pt–Ru/SiO_2 samples were prepared by incipient wetness co-impregnation of the silica support (Grace Davison, XPO-2301, 300 m^2/g) with a mixture of aqueous solutions of $Ru(NO)(NO_3)_3$ and $H_2PtCl_6{\cdot}6H_2O$ (both from Alfa Aesar), followed by drying in air at 120 °C for 12 h. For comparison, Ru/SiO_2 and Pt/SiO_2 samples were also prepared by incipient wetness impregnation of the support with an aqueous solution of the corresponding individual precursors and were dried in air at 120 °C for 12 h. The SiO_2 support was calcined overnight at 500 °C before use. In all cases, the amount of each precursor was chosen to yield samples containing 1.0 wt% of Pt and/or 1.0 wt% of Ru after ligand removal. These Pt and Ru weight loadings were verified in each sample by inductively coupled plasma–mass spectroscopy (ICP-MS) analysis. Due to differences in atomic weight, these 1 wt% loadings for Pt and Ru correspond to a Ru:Pt atomic ratio of approximately 2:1.

Two sets of activation protocols were used to treat samples before further characterization. According to the first set, the dried catalyst was first oxidized in a 5% O_2/N_2 mixture at 300 °C for 2 h and then reduced in a 5% H_2/N_2 mixture at 300 °C for 2 h. Alternatively, the catalyst was directly reduced in the 5% H_2/N_2 mixture at 300 °C for 2 h. The temperature ramp used was 3 °C/min in all cases.

2.2. FTIR spectroscopy

FTIR spectra were collected with a Nicolet Nexus 470 spectrometer equipped with a MCT-B detector cooled by liquid nitrogen. Powder samples were pressed into self-supported wafers with a density of approximately 20 mg/cm^2 and mounted in the IR cell connected to a gas distribution system. Samples were pretreated in situ according to the various activation protocols described above and then cooled to room temperature in flowing He before each measurement. Spectra were recorded at a spectral resolution of 2 cm^{-1}, with 64 scans accumulated per spectrum.

2.3. STEM measurements

STEM images were obtained with a Hitachi HD-2000 instrument with a SEI resolution of 2.4 Å at the operating voltage of 200 keV. Surface-averaged sizes of the metal particles observed were calculated as

$$\frac{\sum_i n_i d_i^3}{\sum_i n_i d_i^2},$$

where n_i is the number of particles with diameter d_i, after measurement of approximately 200 particles from at least 5 different micrographs for each sample [27].

2.4. EXAFS measurements

EXAFS spectra were collected at beamline X-18B at the National Synchrotron Light Source (NSLS), Brookhaven National Laboratory, Upton, NY, and at beamline 2–3 at the Stanford Synchrotron Radiation Laboratory (SSRL), Stanford Linear Accelerator Center, Menlo Park, CA. The storage ring electron energy was 2.8 GeV at NSLS and 3 GeV at SSRL. The ring current was 110–250 mA at NSLS and 80–100 mA at SSRL.

The Pt–Ru/SiO_2 samples in wafer form were loaded into an EXAFS cell [28] connected to a gas manifold, allowing pretreatment of samples according to the procedures described above. After pretreatment, the cell was cooled to room temperature and evacuated to 10^{-5} Torr. The EXAFS data were collected in the transmission mode after the cell had been cooled to nearly liquid nitrogen temperature. Data were collected with a Si(111) double-crystal monochromator detuned by 40% to minimize the effects of higher harmonics in the X-ray beam.

The EXAFS data were analyzed with experimentally and theoretically determined reference files, the former obtained from EXAFS data for materials of known structure. The Pt–Pt, Pt–$O_{support}$, and Ru–$O_{support}$ interactions were analyzed with phase shifts and backscattering amplitudes obtained from EXAFS data for Pt foil, $Na_2Pt(OH)_6$, and RuO_2, respectively. The Ru–Ru, Pt–Ru, and Ru–Pt interactions were analyzed with phase shifts and backscattering amplitudes calculated on the basis of the crystallographic data reported for metallic Ru and [$PtRu_2(CO)_8$(1,2-bis(diphenylphosphino)ethane)] using the FEFF software [29]. The EXAFS parameters were extracted from the raw data with the aid of the XDAP software [30]. The methods used to extract the EXAFS function from the raw data are essentially the same as those reported elsewhere [31]. Data reported for each sample are the averages of five scans.

The raw EXAFS data obtained for the Pt L_3 and Ru K edges were analyzed with a maximum of 16 free parameters over the ranges of $3.50 < k < 15.50$ $Å^{-1}$ (where k is the wave vector) and $0.0 < r < 4.0$ Å (where r is the distance from the absorber atom). The statistically justified number of free parameters, n, was found to be 31, as estimated on the basis of the Nyquist theorem [32,33]: $n = (2\Delta k \Delta r/\pi) + 1$, where Δk and Δr are the k and r ranges used to fit the data. The data analysis was performed with a difference file technique with phase- and amplitude-corrected Fourier transforms of the data [34,35].

The approach used to analyze the data at the Pt L_3 and Ru K edges was similar to that described previously [36]. The Pt–Pt contributions in each sample, the largest in the EXAFS spectra, were estimated first and then subtracted from the raw data. The difference file was expected to represent Pt–$O_{support}$ contributions. After optimizing the parameters for the Pt–$O_{support}$ contributions, the first-guess Pt–Pt and Pt–$O_{support}$ contributions were added and compared with the raw data. The overall fit with the sum of the Pt–Pt and Pt–$O_{support}$ contributions was not satisfactory. The difference files obtained after subtraction of the Pt–Pt and Pt–$O_{support}$ contributions from the raw data indicated the presence of additional high-Z backscatters, which in this case appeared to be Pt–Ru. Therefore, a good fit was obtained when Pt–Pt, Pt–Ru, and Pt–$O_{support}$ contributions were accounted for. The difference files in this case indicated only the presence of noise, showing that no other contributions had to be included in the fit. A similar approach was used to analyze the EXAFS data at the Ru K edge and the best fits were obtained when Ru–Ru, Ru–Pt, and Ru–$O_{support}$ contributions were used for the data analysis. The reliable parameters for the high-Z (Pt, Ru) and low-Z contributions ($O_{support}$) were determined by multiple-shell fitting in r space with application of k^1 and k^3 weightings in the Fourier transformations [31]. Because the EXAFS data were obtained at both the Pt L_3 edge and the Ru K edge, there were opportunities to evaluate the internal consistency of the fitting results. The reliability of the parameters obtained at each edge for Pt–Ru (Ru–Pt) interactions was evaluated on the basis of constraints reported earlier [37] and applied to analysis of bimetallic samples [38].

2.5. Catalytic measurements

Steady-state catalytic activity measurements for the preferential oxidation of CO under excess H_2 were performed in a quartz single-pass fixed-bed microreactor at atmospheric pressure, a gas hourly space velocity (GHSV) of 120,000 ml/(g h), and a reaction feed containing 0.5% CO, 0.5% O_2, 45% H_2, and 54% N_2. The feed and the reaction products were analyzed with on-line single-beam NDIR CO (Ultramat 23, Siemens) and O_2 (Model 201, AMI) analyzers capable of detecting CO and O_2 in the 0–250 ppm and 0–1000 ppm ranges, respectively. The reaction selectivity toward the formation of CO_2 was calculated as the amount of O_2 consumed in the CO oxidation reaction (calculated from the CO balance) over the total amount of O_2 consumed. Additional details of these experiments have been reported elsewhere [39].

3. Results and discussion

3.1. Metal dispersion

Histograms showing the distribution of metal particle sizes for the Ru/SiO_2 and $Pt–Ru/SiO_2$ samples pretreated in H_2 or in O_2/H_2 at 300 °C are shown in Figs. 1 and 2, and the average particle sizes are summarized in Table 1. The results show a substantial effect of the pretreatment procedure on the dispersion of the monometallic Ru/SiO_2 catalysts. More specifically, when the Ru/SiO_2 sample was pretreated in H_2 at 300 °C, all observed metal particles were in the size range of 1–4.5 nm and the surface-averaged size of the Ru particles in this sample was found to be approximately 2.8 nm. However, when an oxidation treatment was used before the reduction step, all particles observed in the STEM images were in the size range of 9–56 nm, and the surface-averaged size was found to be approximately 42 nm, indicating that substantial sintering of Ru took place under these conditions. A similar sintering of Ru after oxidation/reduction treatments was observed earlier for γ-Al_2O_3-supported samples [7], and has been attributed to a weak interaction between Ru and the support, leading to the formation of mobile bulk Ru oxide species under oxidizing conditions that can rapidly sinter upon subsequent reduction [40–42].

When the $Pt–Ru/SiO_2$ sample was exposed to the oxidation/reduction treatment at 300 °C, approximately 99% of the observed metal particles were in the size range of 1–5 nm with the highest occurrence centered at 2.5 nm. In contrast, when the

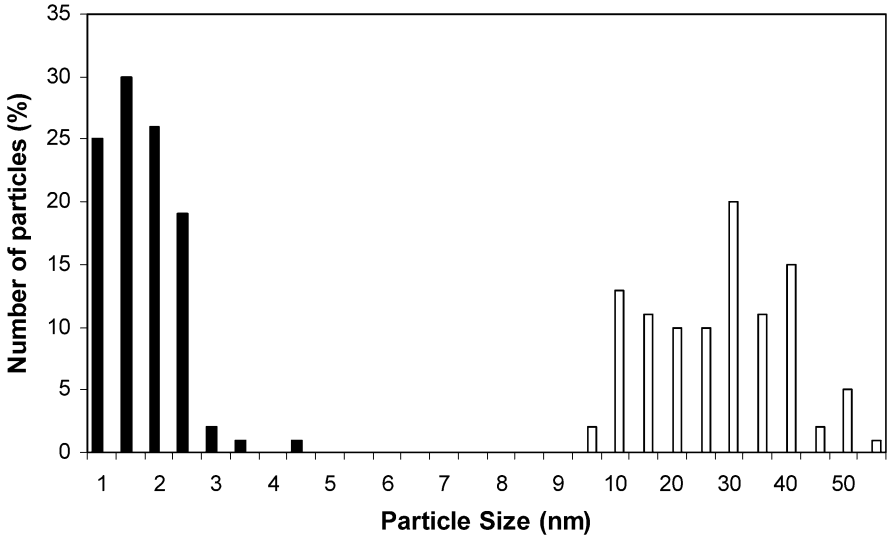

Fig. 1. Particle size distributions characterizing the Ru/SiO_2 sample pretreated in H_2 (■) and in O_2/H_2 (□) at 300 °C.

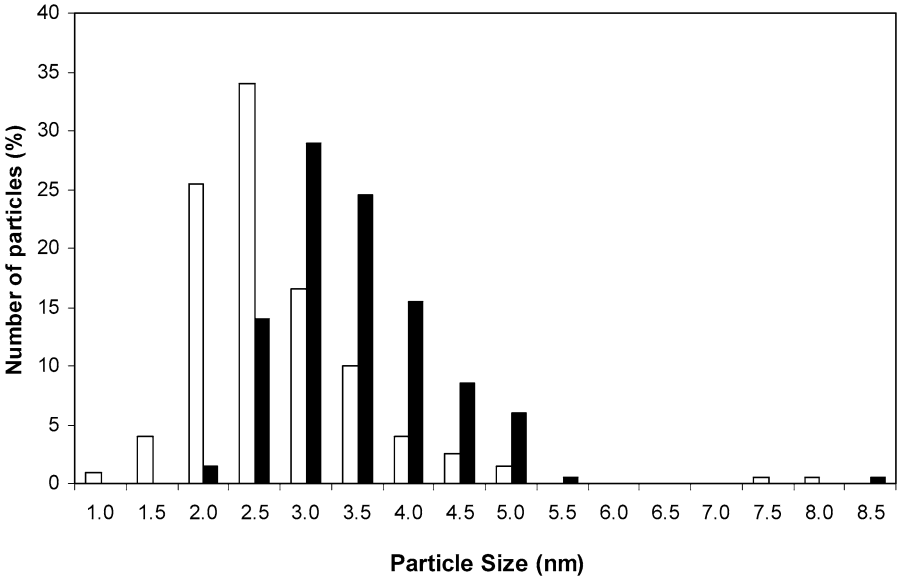

Fig. 2. Particle size distributions characterizing the Pt–Ru/SiO_2 sample pretreated in H_2 (■) and in O_2/H_2 (□) at 300 °C.

Table 1
Average particle sizes estimated from STEM images for Ru/SiO_2 and Pt–Ru/SiO_2 after H_2 and O_2/H_2 treatments at 300 °C

Pretreatment conditions	Sample composition	Average particle size (nm)
5% H_2/N_2 at 300 °C	1% Ru/SiO_2	2.8
	1% Pt–1% Ru/SiO_2	4.1
5% O_2/N_2 at 300 °C followed by 5% H_2/N_2 at 300 °C	1% Ru/SiO_2	42
	1% Pt–1% Ru/SiO_2	3.6

H_2 treatment at 300 °C was used to pretreat the sample, more metal particles of larger sizes were formed. In this case, the majority of observed metal particles were in the size range of 2–5.5 nm, and the highest occurrence was centered at 3.0 nm (Fig. 2). Taking into account only the metal particles located in the size range of 1–5 nm, we may infer that the combination of oxidation/reduction treatments led to a slightly more dispersed bimetallic catalyst than the direct treatment in H_2. However, a further analysis of STEM images indicates that a few particles in the size range of 7–9 nm were also observed after both treatments (Fig. 2). These larger particles account for no more than 1% of the observed particles in both cases, which nevertheless substantially affect the surface-averaged particle sizes shown in Table 1. It is also possible that some very small particles could not be identified in the STEM images and thus were undercounted. However, this should not have a significant effect on the calculated surface-averaged sizes, which are influenced to a much greater extent by larger particles. Because the accuracy in the determination of the surface-averaged sizes can be as high as ±15%, we can conclude that within the margin of error, both treatments resulted in an average particle size of approximately 4.0 nm, indicating that the surface-averaged particle size of the bimetallic Pt–Ru catalysts appears to be rather insensitive to the activation protocol. However, a comparison of the STEM data collected for the Ru/SiO_2 and Pt–Ru/SiO_2 samples clearly shows that the presence of Pt in the catalyst formulation stabilizes the dispersion of Ru in an oxidizing environment. This effect can be attributed to the strong interactions of Pt not only with the support [20], but also with Ru as described below. These strong interactions appear to prevent subsequent sintering of Ru.

3.2. EXAFS evidence of bimetallic interactions

EXAFS results obtained at both the Pt L_3 and Ru K edges for the Pt–Ru/SiO_2 samples pretreated in H_2 or O_2/H_2 at 300 °C are summarized in Table 2. The reported standard deviations for the different parameters were calculated from the covariance matrix using the XDAP software [30].

The Pt L_3 edge EXAFS data characterizing the surface species formed after the pretreatment of Pt–Ru/SiO_2 in H_2 at 300 °C indicate that each Pt atom was in close proximity to approximately 2.8 Ru and 5 Pt atoms at average distances of 2.68 and 2.75 Å, respectively (Table 2). The EXAFS data collected at the Ru K edge for this sample complement those attained at the Pt L_3 edge and show that each Ru atom was in close proximity to approximately 1.4 Pt and 5.2 Ru atoms at average distances of 2.68 and 2.65 Å, respectively. Thus, the EXAFS results at both the Pt L_3 and Ru K edges provide direct evidence for the formation of bimetallic Pt–Ru species on the SiO_2 surface after the H_2 treatment. The observed Pt–Ru distance is exactly the same as that reported earlier for a Pt_2Ru_4/γ-Al_2O_3 sample of organometallic origin [43]. However, to be reliable and consistent, parameters obtained for Pt–Ru bimetallic contributions must satisfy constraints described in detail elsewhere [37] and applied earlier for the EXAFS data analysis of bimetallic samples [38,43]. We can conclude from our data (Table 2) that within expected uncertainties, the Pt–Ru and Ru–Pt bimetallic contributions observed from both edges have similar bond distances and Debye–Waller factors and the ratio of N_{PtRu}/N_{RuPt} is approximately 2, corresponding to the calculated atomic Ru/Pt ratio in the sample. Moreover, the fact

Table 2
EXAFS results at the Pt L_3 and Ru K edges characterizing the surface species formed after the treatment of Pt–Ru/SiO_2 at various conditions[a]

Treatment conditions	Shell	N	R (Å)	$10^3\Delta\sigma^2$ (Å^2)	ΔE_0 (eV)
5% H_2/N_2 at 300 °C	Pt L_3 edge				
	Pt–Pt	5.0 ± 0.1	2.75 ± 0.01	0.0 ± 0.1	−7.2 ± 0.2
	Pt–Ru	2.8 ± 0.1	2.68 ± 0.01	2.2 ± 0.1	2.2 ± 0.1
	Pt–$O_{support}$				
	Pt–O_s	0.7 ± 0.1	2.23 ± 0.01	0.0 ± 0.5	−13.2 ± 0.6
	Pt–O_l	2.2 ± 0.1	2.82 ± 0.01	−2.9 ± 0.2	−6.0 ± 0.2
	Ru K edge				
	Ru–Ru	5.2 ± 0.1	2.65 ± 0.01	2.9 ± 0.1	−1.0 ± 0.1
	Ru–Pt	1.4 ± 0.1	2.68 ± 0.01	2.3 ± 0.2	1.9 ± 0.5
	Ru–$O_{support}$				
	Ru–O_s	1.2 ± 0.1	1.99 ± 0.02	10.0 ± 1.5	−10.6 ± 1.9
	Ru–O_l	1.6 ± 0.1	2.79 ± 0.01	−5.8 ± 0.1	3.7 ± 0.2
5% O_2/N_2 at 300 °C followed by 5% H_2/N_2 at 300 °C	Pt L_3 edge				
	Pt–Pt	3.7 ± 0.1	2.75 ± 0.01	0.0 ± 0.1	−10.0 ± 0.1
	Pt–Ru	4.2 ± 0.1	2.68 ± 0.01	4.7 ± 0.3	−9.5 ± 0.1
	Pt–$O_{support}$				
	Pt–O_s	0.7 ± 0.1	2.23 ± 0.01	0.8 ± 0.3	−12.0 ± 0.2
	Pt–O_l	2.6 ± 0.1	2.82 ± 0.01	−3.5 ± 0.1	−9.5 ± 0.1
	Ru K edge				
	Ru–Ru	5.0 ± 0.1	2.65 ± 0.01	3.7 ± 0.1	−2.3 ± 0.4
	Ru–Pt	2.3 ± 0.2	2.68 ± 0.01	4.6 ± 0.2	1.0 ± 0.7
	Ru–$O_{support}$				
	Ru–O_s	0.9 ± 0.1	2.01 ± 0.03	10.0 ± 4.0	−14.5 ± 4.1
	Ru–O_l	2.3 ± 0.1	2.78 ± 0.01	−3.2 ± 0.2	2.5 ± 0.5

[a] Notation: N, coordination number; R, distance between absorber and backscatterer atom; $\Delta\sigma^2$, Debye–Waller factor, which is relative to the Debye–Waller factor of the reference compound; ΔE_0, inner potential correction accounting for the difference in the inner potential between the sample and the reference compound; the subscripts s and l refer to short and long, respectively. Standard deviations were calculated from the covariance matrix using the XDAP software [29].

that the Pt–Ru bond distance of 2.68 Å is very close to the value of 2.70 Å calculated from the sum of the radii of the observed Pt–Pt and Ru–Ru contributions is an additional argument strengthening the internal consistency of the EXAFS data obtained [43].

When the Pt–Ru/SiO_2 sample was exposed to the oxidation/reduction treatment at 300 °C, the EXAFS data collected at the Pt L_3 edge show that each Pt atom was in close proximity to approximately 4.2 Ru and 3.7 Pt atoms at average distances of 2.68 and 2.75 Å, respectively. Similar data obtained from the Ru K edge for this sample indicate the presence of approximately 2.3 Pt and 5 Ru atoms at average distances of 2.68 and 2.65 Å, respectively, in close proximity to each Ru atom (Table 2). Once again, the parameters characterizing the Pt–Ru bimetallic contributions within expected uncertainties satisfy the constraints mentioned above, demonstrating the reliability of the data obtained.

In summary, an important result clearly demonstrated by the EXAFS data at both the Pt L_3 and Ru K edges is the formation of Pt–Ru bimetallic species on the SiO_2 surface after the H_2 and O_2/H_2 treatments. Furthermore, the number of neighboring Pt and Ru atoms was higher in the sample that underwent an O_2 treatment first (Table 2). As a result, the calculated fraction of bimetallic contributions in this sample was also higher after such treatment (Table 3), indicating that the combination of oxidation/reduction treatments promotes the formation of bimetallic species. These increased interactions between Pt and Ru atoms likely limited the mobility of Ru after the oxidation/reduction treatment, thus preventing its sintering.

Table 3
Fraction of bimetallic contributions estimated for the Pt–Ru/SiO_2 sample after H_2 and O_2/H_2 treatments at 300 °C

Pretreatment conditions	$N_{Pt-Ru}/(N_{Pt-Pt} + N_{Pt-Ru})$	$N_{Ru-Pt}/(N_{Ru-Ru} + N_{Ru-Pt})$
5% H_2/N_2 at 300 °C	0.36	0.20
5% O_2/N_2 at 300 °C followed by 5% H_2/N_2 at 300 °C	0.53	0.31

3.3. EXAFS evidence of metals segregation

As mentioned in the preceding section, analysis of the EXAFS data indicates that along with the Pt–Ru bimetallic contributions, Pt–Pt and Ru–Ru contributions were also present (Table 2). Taking into account that EXAFS provides average information throughout the bulk of the catalyst and in the absence of detailed characterization of the composition of observed individual nanoparticles, we can only speculate regarding the origin of the observed Pt–Pt and Ru–Ru contributions. First, because a conventional incipient wetness co-impregnation technique was used to prepare the Pt–Ru/SiO_2 samples, the presence of these contributions could indicate that not all Pt and Ru atoms are present in bimetallic particles. Therefore, it would

be possible that some Pt and Ru atoms have formed small monometallic clusters on the SiO_2 surface. In such a case, the appearance of Pt–Pt and Ru–Ru contributions would be expected in the EXAFS data; however, Pt and Ru are miscible in a wide range of Pt/Ru ratios, and the formation of bulk PtRu alloys is well documented in the literature [44]. Moreover, the synthesis of PtRu bimetallic catalysts on various supports from molecular $PtRu_5C(CO)_6$ and $Pt_2Ru_4(CO)_{18}$ cluster precursors has been reported [43,45–47]. Precise structural characterization of such nearly uniform cluster-derived samples by EXAFS revealed not only the presence of Pt–Ru and Ru–Pt interactions in the local coordination environments of Pt and Ru, but also the presence of Pt–Pt and Ru–Ru contributions [43,45–47]. At the same time, the EDX analysis reported for these samples indicates that all observed particles were bimetallic in nature, with composition nearly identical to that of the bimetallic cluster precursors, and no evidence was found to indicate segregation of Pt and Ru into monometallic nanoparticles [45]. Therefore, the available literature data indicate that Pt and Ru atoms in bimetallic nanoparticles can be located not only in an atomically mixed phase that yields Pt–Ru (or Ru–Pt) contributions, but also in partially segregated phases leading to the appearance of Pt–Pt and Ru–Ru contributions in the EXAFS data, consistent with our observations.

Our EXAFS data (Table 2) further indicate that the pretreatment conditions have no substantial effect on the segregation of Ru in the Pt–Ru/SiO_2 samples, because an average Ru–Ru coordination number of approximately 5 was observed after both the H_2 and O_2/H_2 treatments. However, the average Pt–Pt coordination numbers were 3.7 and 5 after the O_2/H_2 and H_2 treatments, respectively, suggesting a greater tendency for Pt to segregate during the direct H_2 treatment. The EXAFS data alone do not allow us to determine whether the segregation of Pt and Ru occurs throughout the bulk of the bimetallic particles or toward the surface of the particles with a preference for the formation of Pt–Ru bonds at the interface. Analysis of the low-Z contributions also does not clarify the picture, because the EXAFS data clearly show that both Pt and Ru are interacting with the support to a similar extent, as evidenced by the presence of both Pt–$O_{support}$ and Ru–$O_{support}$ contributions in the spectra (Table 2). However, previous literature reports indicate that Ru has a tendency to segregate toward the core of the particles, whereas Pt segregates toward the surface in both supported Pt–Ru catalysts [17,19,45,46] and bulk Pt–Ru systems [48].

Finally, the average metal coordination numbers estimated from the EXAFS data can be used to approximate the average size of the nanoparticles formed using different models described in the literature [49,50]. Typically, such estimates correlate closely with corresponding electron microscopy, hydrogen chemisorption, or X-ray diffraction line-broadening data for both the monometallic and bimetallic samples [51–53]. In our case, however, the weighted average coordination numbers, calculated as $N_{M-M} = (N_{Pt-M} + 2N_{Ru-M})/3$ based on the Pt/Ru atomic ratio, were found to be 7.5 and 7 after O_2/H_2 and H_2 treatments, respectively, slightly lower than the N_{M-M} coordination number of approximately 10 expected for an average particle size of 4 nm [50]. This difference can be attributed to shape variations of the surface species. More specifically, some of the Pt–Ru surface species formed can have a raft-like geometry, resulting in a reduced total N_{M-M} coordination for the first shell. In such a case, the average total N_{M-M} coordination determined experimentally by EXAFS would be lower than the anticipated values for the three-dimensional particles due to a larger fraction of lower coordination sites present, consistent with our observations. In fact, the formation of bimetallic rafts has been also suggested for RuCu/SiO_2 catalysts [54].

3.4. Infrared spectra of CO adsorbed on Pt–Ru/SiO_2

Fig. 3 shows IR spectra collected at room temperature after exposure of the pretreated Pt–Ru/SiO_2 samples to 1% CO/He.

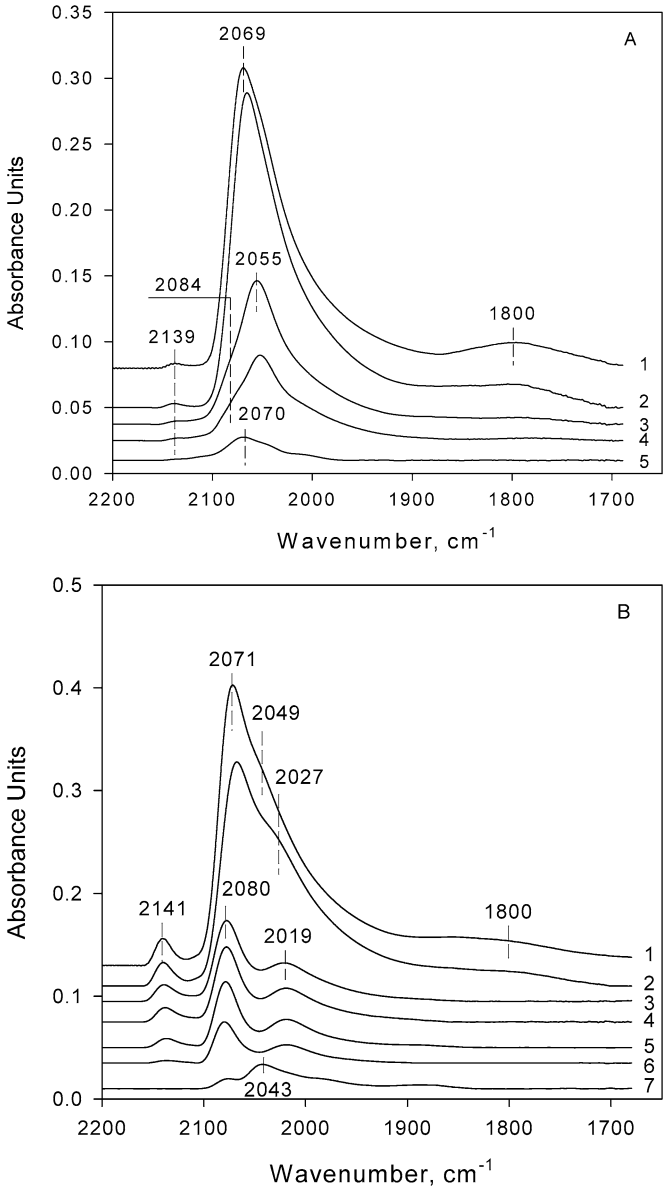

Fig. 3. FTIR spectra in the ν_{CO} region of the Pt–Ru/SiO_2 sample pretreated at 300 °C in (A) O_2/H_2 and (B) H_2 collected after adsorption of CO at room temperature (1) and subsequent flushing in He for (2) 1 min at 25 °C, (3) 20 min at 25 °C, (4) at 70 °C, (5) at 110 °C, (6) at 150 °C, (7) at 210 °C.

When the sample was pretreated in O_2/H_2 at 300 °C (Fig. 3A, spectrum 1), the adsorption of CO at room temperature led to the appearance of a strong band at 2069 cm^{-1} with tailing at the lower-frequency side. A weak band at 2139 cm^{-1} and a broad feature in the 1900–1700 cm^{-1} region are also visible in the spectrum. Immediately after the removal of gas-phase CO, the strong band at 2069 cm^{-1} slightly downshifted to 2066 cm^{-1}, while the other features remained intact (Fig. 3A, spectrum 2). However, on flushing with He at room temperature for 20 min, the intensity of the strong band at 2066 cm^{-1} decreased substantially, whereas the band shifted further to 2055 cm^{-1} (Fig. 3A, spectrum 3). With the diminished intensity of this strong band, a shoulder at 2084 cm^{-1} became clearly discernible. The intensity of all bands decreased further with increasing temperature to 110 °C, and finally, only a weak absorption band at 2070 cm^{-1} with a tail ranging to approximately 2000 cm^{-1} remained in the spectrum at 210 °C (Fig. 3A, spectrum 5).

When the Pt–Ru/SiO_2 sample was pretreated in H_2 at 300 °C, a similar trend was observed after exposure to the 1% CO/He mixture at room temperature. Once again, a strong band was observed at 2071 cm^{-1}, a weak band at 2141 cm^{-1}, and a broad feature in the 1900–1700 cm^{-1} region (Fig. 3B, spectrum 1). In this case, however, a shoulder at approximately 2049 cm^{-1} was also present at the lower-frequency side of the 2071-cm^{-1} band. In addition, the band at 2141 cm^{-1} was substantially stronger than the similar band observed with the sample pretreated in O_2/H_2. After flushing with He, the strong band at 2071 cm^{-1} downshifted slightly to 2068 cm^{-1}, and a shoulder at approximately 2027 cm^{-1} became discernible. Similar to the previous sample, the band at 2068 cm^{-1} decreased rapidly in intensity and almost completely disappeared from the spectrum after 20 min of flushing with He at room temperature, leaving three weaker bands at 2141, 2080, and 2019 cm^{-1} in the spectrum (Fig. 3B, spectrum 3). With increasing temperature, all three bands decreased in intensity, and eventually, at 210 °C, the band at 2141 cm^{-1} disappeared from the spectrum and a new band at 2043 cm^{-1} with a tail in the 1980 cm^{-1} region became discernible (Fig. 3B, spectrum 7).

The strong band observed in the spectra of both samples at approximately 2070 cm^{-1} can be assigned to CO adsorbed linearly on Pt [55], whereas the shoulder at 2049 cm^{-1} observed with the sample pretreated in H_2 can be assigned to a similar CO species adsorbed on Ru [56]. The band at approximately 2140 cm^{-1} can be assigned to the symmetric vibration of a tricarbonyl species adsorbed on partially oxidized Ru^{n+} sites formed via oxidative disruption of finely dispersed Ru clusters with the participation of hydroxyl groups from the support [56–58]. The presence of this band is accompanied by the corresponding asymmetric band at 2080 cm^{-1}, which is clearly visible in the spectra of the sample pretreated in H_2 after desorption of the CO from Pt (Fig. 3B, spectra 3–7), and appears as a low-intensity shoulder in the spectra of the sample pretreated in O_2/H_2 (Fig. 3A, spectra 2–4). The appearance of these bands suggests that the tricarbonyl species are present on both surfaces, although the concentration of such species was much lower when the O_2/H_2 treatment was used. Several other CO species adsorbed on metallic Ru, such as different types of tricarbonyls and dicarbonyls, together with a monocarbonyl species adsorbed on partially oxidized Ru^{n+} sites also have been known to contribute to IR features in the 2080 cm^{-1} region [56]. Among these species, dicarbonyls would also have symmetric and asymmetric stretching bands at approximately 2080 and 2020 cm^{-1} [56]. The presence of the band at 2020 cm^{-1} in the spectrum of the sample pretreated in H_2 suggests that such species were also present on this surface, although this does not appear to be the case with the sample that underwent O_2/H_2 treatment. Furthermore, all three bands at 2141, 2080, and 2019 cm^{-1} did not experience significant shifts with increasing temperature (i.e., decreasing surface coverage), suggesting that the corresponding CO species are isolated, in agreement with the above assignments. These results also suggest that the band at 2080 cm^{-1} most likely did not include a contribution from multi-carbonyls adsorbed on metallic Ru, because the nonisolated nature of such species would lead to frequency shifts with surface coverage due to dipole–dipole coupling [56]. The band at 2043 cm^{-1} observed in the spectrum of the sample pretreated only in H_2 (Fig. 3B, spectrum 7) can result from a conversion of tricarbonyl to dicarbonyl species at higher temperatures. Nevertheless, this band can also arise from rearrangements of terminal carbonyls at higher temperatures on the less-densely populated Ru^0 to a more stable form of dicarbonyl adsorption, as evidenced by its asymmetric component in the 1980 cm^{-1} region [56]. Finally, the band in the lower-frequency region (i.e., 1900–1700 cm^{-1}) can be assigned to bridged–bonded CO species [55,56]. In this case, it is not possible to distinguish whether these species are bonded only to Ru, only to Pt, or to both Ru and Pt.

CO adsorbed on SiO_2- and Al_2O_3-supported Pt is known to be highly stable and to remain on the Pt surface at temperatures above 300 °C [55,59]. Similarly, CO species adsorbed on monometallic Ru samples have moderate stability and are known to remain on the Ru surface at temperatures up to 200–250 °C [56]. Our results indicate that regardless of the pretreatment conditions, the CO adsorbed on the Pt sites of the Pt–Ru/SiO_2 samples (band at approximately 2070 cm^{-1}) is weakly bound to the surface. Most of it desorbs with flushing in He at room temperature, with the remaining amount completely removed from the surface at approximately 70–100 °C. A similar effect was also observed with the CO species bonded linearly on Ru sites as the shoulder at approximately 2040 cm^{-1} was removed from the spectrum upon flushing in He even at room temperature. These results indicate that the surface properties of both metals, particularly the strength of the CO–M bond, have been modified by the presence of the other metal (i.e., the CO–M bond has been weakened in both cases), which is consistent with literature reports demonstrating a substantial decrease in the CO adsorption energy on bimetallic Pt/Ru surfaces [60]. In addition, the characteristic ν_{CO} band for the monometallic Pt/SiO_2 sample has been observed at approximately 2078 cm^{-1} [61], whereas in the case of Pt–Ru/SiO_2, this band was located at approximately 2069–2071 cm^{-1} (Fig. 3). Such a red shift may also suggest the presence of electronic interactions between Pt and Ru in the bimetallic sample, leading to a possible

redistribution of the electron density in the two metals. Such a suggestion is also consistent with the EXAFS results demonstrating the presence of a strong bimetallic Pt–Ru character in the Pt–Ru/SiO_2 samples treated at different conditions.

The CO adsorption results further suggest a greater extent of interparticle segregation (i.e., segregation of the two metals into individual particles) for the sample pretreated only in H_2. The appearance of the bands at 2140, 2080, and 2019 cm^{-1} in this case indicates the presence of isolated Ru sites that allow the formation of multicarbonyl species. Moreover, the stability of these species appears to remain unmodified from monometallic Ru [56], suggesting that these sites are not interacting with Pt.

Interparticle segregation was observed to a much lesser extent with the sample treated in O_2/H_2, as evidenced by the much lower intensity of the Ru tricarbonyl band at 2140 cm^{-1}. This indicates that the oxidation treatment before the reduction treatment promoted interactions between Pt and Ru in this sample, consistent with the EXAFS findings. Previous reports have shown contradicting results, claiming that an O_2 treatment leads to increased segregation in Pt–Ru systems [17,22]. However, such conclusions were based on EDX results collected from fewer than 30 individual particles and hence may not be sufficiently representative of the entire sample.

Finally, it appears that the segregation of Pt toward the surface of the nanoparticles formed was more pronounced for the Pt–Ru/SiO_2 sample treated in O_2/H_2. It is possible that a small fraction of Ru remained on the surface after such treatment, but the characteristic absorption band of CO on Ru, which is expected to be observed in the 2040–2050 cm^{-1} region, was not apparent in the spectra. It has been reported previously that the surface of supported Pt–Ru catalysts is enriched with Pt even after reduction in H_2, and that previous oxidation treatment results in further surface enrichment of Pt [19]. Our results appear to be consistent with these earlier findings.

3.5. Activity measurements

CO conversion versus temperature curves obtained for the PROX reaction over Pt–Ru/SiO_2, Pt/SiO_2, and Ru/SiO_2 catalysts pretreated in O_2/H_2 and H_2 are shown in Fig. 4. When the Ru/SiO_2 sample was pretreated in H_2, complete elimination of CO (i.e., outlet CO concentration <1 ppm) was observed in the temperature range of 120–160 °C under the conditions examined. In this case, the O_2 conversion curve proceeded in parallel to that of CO, with both curves reaching 100% conversion simultaneously. A further increase in temperature beyond 160 °C resulted in decreased CO conversion due to the increased rate of the competing H_2 oxidation reaction at elevated temperatures and the possible onset of the reverse water–gas shift reaction, which generates CO. However, it has been reported that in the absence of O_2, the reverse water–gas shift reaction proceeds with appreciable rates only at temperatures above 300 °C on Pt [62,63] and above 200 °C on Ru [64]. When the Ru/SiO_2 sample was exposed to the O_2/H_2 treatment, the O_2 and CO conversion curves were no longer parallel to each other. In this case, the consumption of O_2 was faster than that of CO, with 100% O_2 conversion reached at approximately 170 °C but only 30% CO conversion achieved at 200 °C. These results can be attributed to the sintering of Ru in this sample after the O_2/H_2 treatment at 300 °C, which results in a significantly lower number of surface Ru atoms capable of activating CO molecules. In contrast, the oxidation of H_2 does not appear to be affected as much, and complete conversion of O_2 is still observed below 200 °C. This suggests that the large Ru surfaces present in the larger Ru particles formed after the O_2/H_2 treatment favor the oxidation of H_2 over that of CO.

As indicated by the results shown in Fig. 4, Pt/SiO_2 can effectively and selectively oxidize CO in the presence of hydrogen at much higher temperatures than Ru/SiO_2. More specifically, under the conditions studied a measurable conversion of CO was observed over Pt/SiO_2 only at temperatures above 150 °C, and complete elimination of CO was achieved at approximately 250 °C. The conversions of CO and O_2 increased in parallel as the reaction temperature was increased to 250 °C, yielding a selectivity of approximately 50%. A further increase in the reaction temperature to 280 °C was accompanied by a decrease in the CO conversion to approximately 90%, while the O_2 conversion remained at 100%. These results demonstrate that Pt/SiO_2 has a fairly narrow temperature window of operation for CO elimination under PROX conditions, consistent with previous literature reports [39,65].

When the bimetallic Pt–Ru/SiO_2 catalyst was directly reduced in H_2 at 300 °C, its catalytic behavior was similar to that of monometallic Ru/SiO_2 pretreated under similar conditions. This result is consistent with our IR data suggesting that a substantial fraction of Ru atoms remains exposed on the surface of the Pt–Ru/SiO_2 catalyst after such treatment. In contrast, when the same bimetallic catalyst underwent O_2/H_2 treatment at 300 °C, a delay of approximately 30 °C was observed in the CO light-off temperature. Such a delay, signifying decreased CO oxidation activity, can be related to a decreased fraction of Ru sites available on the surface of this sample, because the FTIR data suggest that the surface of the metal nanoparticles formed after such treatment is enriched with Pt. Given the relatively small fraction of exposed Ru sites, we should also consider that the bimetallic interaction between Pt and Ru may have substantially enhanced the activity of Pt for PROX. Such an enhancement can be attributed to the lower strength of CO adsorption, as indicated by the FTIR measurements. Strong interaction of CO with noble metals leads to an operating surface predominantly saturated with CO, even in the presence of H_2 or O_2. Hence, the onset of CO oxidation is controlled by the surface coverage of CO, which limits the number of vacant sites for O_2 adsorption and dissociation. Such a model is established on the assumption that competitive adsorption occurs between CO and O_2 and has previously been proposed by others [66,67]. Hence, the lower strength of CO adsorption in the case of the Pt–Ru sample could promote the oxidation of CO on Pt.

Complete conversion of CO was never achieved with the Pt–Ru/SiO_2 sample that underwent O_2/H_2 treatment at 300 °C. As shown in Fig. 4, the CO conversion decreased immediately after reaching its maximum value of approximately 95% at 140 °C. Once again, this may be due to the decrease strength of CO adsorption, at elevated temperatures. As a result, at the onset

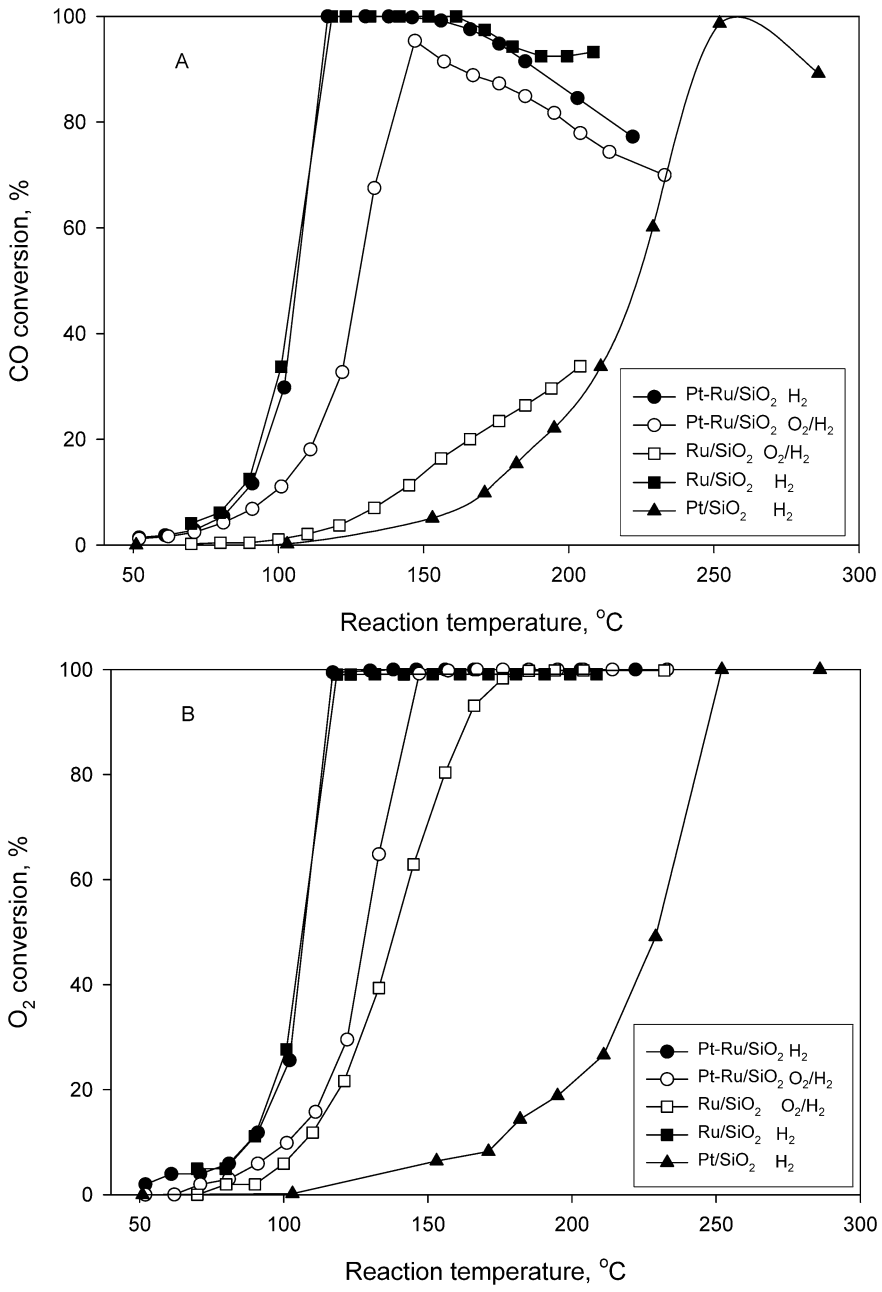

Fig. 4. CO (A) and O_2 (B) conversions at different temperatures under PROX conditions over various SiO_2-supported catalysts pretreated at 300 °C in O_2/H_2 (open symbols) or H_2 (closed symbols): Ru (□, ■), Pt–Ru (○, ●), and Pt (▲). (Reaction conditions: 0.5% CO, 0.5% O_2, 45% H_2, balance N_2, space velocity 120,000 ml/(g h).)

of the partial desorption of CO at relatively low temperatures, the vacated active sites allow for H_2 chemisorption to proceed more easily, and hence lead to a higher rate of H_2 oxidation.

4. Conclusion

The effects of pretreatment conditions (i.e., consecutive treatments in O_2/H_2 and direct treatment only in H_2) on the structural properties and activity of SiO_2-supported bimetallic Pt–Ru catalysts for the selective oxidation of CO were investigated. The results indicate that the presence of Pt stabilizes Ru and prevents its sintering during exposure to oxidizing conditions. Furthermore, the strength of the CO adsorption on the bimetallic samples is lower than that on the monometallic counterparts, presumably due to the presence of bimetallic interactions between Pt and Ru. The use of an O_2/H_2 treatment increases the Pt–Ru bimetallic interactions, and thus a lower degree of phase segregation between Pt and Ru is observed in this case. However, intraparticle segregation (i.e., segregation of the two metals within the same particle) is more pronounced after this treatment with the surface of the nanoparticles formed being substantially enriched in Pt. In contrast, significant amounts of both Pt and Ru are present on the surface of samples pretreated directly in H_2. Such samples exhibit similar activity for the PROX reaction to that of monometallic Ru, since a sufficient number of Ru sites appear to be present on their surface

to drive the reaction. No added benefit from the presence of Pt was observed in this case. Only a very small fraction of Ru sites was present on the surface of Pt–Ru samples treated in O_2/H_2, and hence, catalytic behavior similar to that of Pt would be expected. However, the activity of such samples is substantially improved over that of Pt, most probably due to the lower strength of adsorption of CO on Pt, which can be attributed to the Pt–Ru interactions.

Acknowledgments

The authors gratefully acknowledge the financial support of the U.S. Department of Energy (DE-FG02-96ER14666). STEM experiments at the Oak Ridge National Laboratory (ORNL) were sponsored by the Division of Materials Sciences and Engineering and by the Assistant Secretary for Energy Efficiency and Renewable Energy, Office of FreedomCAR and Vehicle Technologies, as part of the High-Temperature Materials Laboratory User Program, Oak Ridge National Laboratory, managed by UT-Battelle, LLC, for the U.S. Department of Energy under contract number DE-AC05-00OR22725. Use of the National Synchrotron Light Source, Brookhaven National Laboratory, was supported by the U.S. Department of Energy, Office of Science, Office of Basic Energy Sciences, under contract DE-AC02-98CH10886. Portions of this research were also carried out at the Stanford Synchrotron Radiation Laboratory, a national user facility operated by Stanford University on behalf of the U.S. Department of Energy, Office of Basic Energy Sciences. We are grateful to the beamline staff at both facilities for their assistance. The authors also acknowledge Dr. Lorna Soto for assistance with the STEM measurements, and useful discussions with Dr. Markus Hoelzle and Mr. David Artrip (BASF).

References

[1] M. Haruta, S. Tsubota, in: A. Wieckowski, E.R. Savinova, C.G. Vayenas (Eds.), Catalysis and Electrocatalysis at Nanoparticle Surfaces, Marcel Dekker, New York, 2003, p. 645.
[2] E. McCarthy, J. Zahradnik, G.C. Kuczynski, J.J. Carberry, J. Catal. 39 (1975) 29.
[3] A. Golchet, J.M. White, J. Catal. 53 (1978) 266.
[4] Y. Nishiyama, H. Wise, J. Catal. 32 (1974) 50.
[5] S.H. Oh, G.B. Fisher, J.E. Carpenter, D.W. Goodman, J. Catal. 100 (1986) 360.
[6] M.J. Kahlich, H.A. Gasteiger, R.J. Behm, J. Catal. 171 (1997) 93.
[7] S.Y. Chin, O.S. Alexeev, M.D. Amiridis, Appl. Catal. 286 (2005) 157.
[8] M. Echigo, T. Tabata, Catal. Lett. 98 (2004) 37.
[9] A. Wörner, C. Friedrich, R. Tamme, Appl. Catal. A 245 (2003) 1.
[10] Y.-F. Han, M.J. Kahlich, M. Kinne, R.J. Behm, Appl. Catal. B 50 (2004) 209.
[11] P.V. Snytnikov, V.A. Sobyanin, V.D. Belyaev, P.G. Tsyrulnikov, N.B. Shitova, D.A. Shlyapin, Appl. Catal. A 239 (2002) 149.
[12] Y.-F. Han, M.J. Kahlich, M. Kinne, R.J. Behm, Phys. Chem. Chem. Phys. 4 (2002) 389.
[13] P.V. Snytnikov, V.A. Sobyanin, V.D. Belyaev, D.A. Shlyapin, Khim. Interesakh Ustoichivogo Razvitiya 11 (2003) 297.
[14] H. Miura, R.D. Gonzalez, J. Catal. 74 (1982) 216.
[15] G. Diaz, F. Garin, G. Maire, S. Alerasool, R.D. Gonzalez, Appl. Catal. A 124 (1995) 33.
[16] P. Ramamoorthy, R.D. Gonzalez, J. Catal. 58 (1979) 188.
[17] S. Alerasool, R.D. Gonzalez, J. Catal. 124 (1990) 204.
[18] P. Esteban, G. Diaz, L. Guczi, F. Garin, P. Bernhardt, J.L. Schmitt, G. Maire, J. Chem. Phys. 86 (1989) 1727.
[19] H. Miura, T. Suzuki, Y. Ushikubo, K. Sugiyama, T. Matsuda, R.D. Gonzalez, J. Catal. 85 (1984) 331.
[20] S. Alerasool, D. Boecker, B. Rejai, R.D. Gonzalez, Langmuir 4 (1988) 1083.
[21] G.D. Angel, C. Medina, R. Gomez, B. Rejai, R.D. Gonzalez, Catal. Today 5 (1989) 395.
[22] G.D. Angel, V. Bertin, P. Bosch, R. Gomez, R.D. Gonzalez, New J. Chem. 15 (1991) 643.
[23] T. Miyao, M. Yamauchi, S. Naito, Catal. Today 87 (2003) 227.
[24] A.S. Aricò, P.L. Antonucci, E. Modica, V. Baglio, H. Kim, V. Antonucci, Electrochim. Acta 47 (2002) 3723.
[25] V. Radmilović, H.A. Gasteiger, P.N. Ross Jr., J. Catal. 154 (1995) 98.
[26] P.N. Ross, Electrochim. Acta 36 (1991) 2053.
[27] V.I. Zaikovskii, Yu.A. Ryndin, V.I. Kovalchuk, L.M. Plyasova, B.N. Kuznetsov, Yu.I. Yermakov, Kinet. Katal. 22 (1981) 443.
[28] R.E. Jentoft, S.E. Deutsch, B.C. Gates, Rev. Sci. Instrum. 67 (1996) 2111.
[29] J.J. Rehr, J. Mustre de Leon, S.I. Zabinsky, R.C. Albers, J. Am. Chem. Soc. 113 (1991) 5135.
[30] M. Vaarkamp, J.C. Linders, D.C. Koningsberger, Physica B 208–209 (1995) 159.
[31] D.C. Koningsberger, in: C.A. Melendres, A. Tadjeddine (Eds.), Synchrotron Techniques in Interfacial Electrochemistry, Kluwer, Dordrecht, 1994, p. 181.
[32] E.A. Stern, Phys. Rev. B 48 (1993) 9825.
[33] E.O. Brigham, The Fast Fourier Transform, Prentice–Hall, Englewood Cliffs, NJ, 1974.
[34] P.S. Kirlin, F.B.M. van Zon, D.C. Koningsberger, B.C. Gates, J. Phys. Chem. 94 (1990) 8439.
[35] J.B.A.D. van Zon, D.C. Koningsberger, H.F.J. van't Blik, D.E. Sayers, J. Chem. Phys. 82 (1985) 5742.
[36] O. Alexeev, M. Shelef, B.C. Gates, J. Catal. 164 (1996) 1.
[37] G.H. Via, K.F. Drake, G. Meitzner, F.W. Lytle, J.H. Sinfelt, Catal. Lett. 5 (1990) 25.
[38] O.S. Alexeev, G.W. Graham, M. Shelef, B.C. Gates, J. Catal. 190 (2000) 157.
[39] O.S. Alexeev, S.Y. Chin, M.H. Engelhard, L. Ortiz-Soto, M.D. Amiridis, J. Phys. Chem. B 109 (2005) 23430.
[40] G.C. Bond, J.C. Slaa, J. Mol. Catal. A 96 (1995) 163.
[41] G.C. Bond, J.C. Slaa, J. Mol. Catal. 89 (1994) 221.
[42] B. Coq, E. Crabb, M. Warawdekar, G.C. Bond, J.C. Slaa, S. Galvagno, L. Mercadante, J.G. Ruiz, M.C.S. Sierra, J. Mol. Catal. 92 (1994) 107.
[43] O.S. Alexeev, G.W. Graham, M. Shelef, R.D. Adams, B.C. Gates, J. Phys. Chem. B 106 (2002) 4697.
[44] H.A. Gasteiger, N. Markovic, P.N. Ross, E.J. Cairns, J. Phys. Chem. 97 (1993) 12020.
[45] M.S. Nashner, A.I. Frenkel, D.L. Adler, J.R. Shapley, R.G. Nuzzo, J. Am. Chem. Soc. 119 (1997) 7760.
[46] M.S. Nashner, A.I. Frenkel, D. Somerville, C.W. Hills, J.R. Shapley, R.G. Nuzzo, J. Am. Chem. Soc. 120 (1998) 8093.
[47] C.W. Hills, M.S. Nashner, A.I. Frenkel, J.R. Shapley, R.G. Nuzzo, Langmuir 15 (1999) 690.
[48] H.A. Gasteiger, P.N. Ross, E. Cairns, J. Surf. Sci. 293 (1993) 67.
[49] R.B. Greegor, F.W. Lytle, J. Catal. 63 (1980) 476.
[50] B.J. Kip, F.B.M. Duivenvoorden, D.C. Koningsberger, R. Prins, J. Catal. 105 (1987) 26.
[51] K.I. Pandya, S.M. Heald, J.A. Hriljac, L. Petrakis, J. Fraissard, J. Phys. Chem. 100 (1996) 5070.
[52] E.S. Shpiro, R.W. Joyner, K.M. Minachev, P.D.A. Pudney, J. Catal. 127 (1991) 366.
[53] B.S. Clausen, L. Gråbæk, H. Topsøe, L.B. Hansen, P. Stoltze, J.K. Nørskov, O.H. Nielsen, J. Catal. 141 (1993) 368.
[54] J.H. Sinfelt, G.H. Via, F.W. Lytle, J. Chem. Phys. 72 (1980) 4832.
[55] R. Barth, R. Pitchai, R.L. Anderson, X.E. Verykios, J. Catal. 116 (1989) 61.
[56] S.Y. Chin, C.T. Williams, M.D. Amiridis, J. Phys. Chem. B 110 (2006) 871.

[57] G.H. Yokomizo, C. Louis, A.T. Bell, J. Catal. 120 (1989) 1.
[58] J.L. Robbins, J. Catal. 115 (1989) 120.
[59] O. Alexeev, D.-W. Kim, G.W. Graham, M. Shelef, B.C. Gates, J. Catal. 185 (1999) 170.
[60] F. Buatier de Mongeot, M. Scherer, B. Gleich, E. Kopatzki, R.J. Behm, Surf. Sci. 411 (1998) 249.
[61] C. Mihut, C. Descorne, D. Duprez, M.D. Amiridis, J. Catal. 212 (2002) 125.
[62] D.H. Kim, M.S. Lim, Appl. Catal. A Gen. 224 (2002) 27.
[63] B.I. Whittington, C.J. Jiang, D.L. Trimm, Catal. Today 26 (1995) 41.
[64] S.Y. Chin, unpublished results.
[65] D.J. Suh, C. Kwak, J.-H. Kim, S.M. Kwon, T.-J. Park, J. Power Sources 142 (2005) 70.
[66] N.W. Cant, R.A. Donaldson, J. Catal. 71 (1981) 320.
[67] J. Szanyi, D.W. Goodman, J. Phys. Chem. 98 (1994) 2972.